Non-linear Numerical Modeling of Partially Pre-stressed Beam-column Sub-assemblages Made of Reactive Powder Concrete

Bambang Budiono[1], Siti Aisyah Nurjannah[2*], & Iswandi Imran[1]

[1]Structure Research Group, Civil Engineering Department,
Faculty of Civil and Environmental Engineering, Institut Teknologi Bandung,
Jalan Ganesha No. 10, Bandung 40132, Indonesia
[2]Civil Engineering Department, Universitas Sriwijaya,
Jalan Raya Palembang – Prabumulih km 32 Indralaya, Indonesia
*E-mail: sanurjannah@gmail.com

Abstract. Three partially pre-stressed interior beam-column sub-assemblages (SI) and two partially pre-stressed exterior beam-column sub-assemblages (SE) made of reactive powder concrete as test specimens were numerically modeled using a finite element program. The objective of this study was to investigate the behavior of the SI and SE numerical models. The numerical model inputs were: material data, details of test specimen dimensions, and test specimen reinforcements. The numerical models were subjected to the same loads as those applied experimentally. The numerical modeling results were hysteretic and backbone curves and stress distribution contours. The numerical model outputs showed good similarity with the experimental results. The stress distribution contours of the numerical models correlated with the crack patterns in the joint zone of the test specimens. The behavior of the SI numerical models differed from the SE numerical models due to various stresses on the beam plastic joints and the joint zones.

Keywords: *crack pattern; finite element numerical model; partially pre-stressed; reactive powder concrete; stress distribution.*

1 Introduction

Five partially pre-stressed beam-column sub-assemblage test specimens were numerically modeled to investigate the hysteretic curves, stress distribution contours, and their relation to the behavior of the test specimens. The concrete material used for all test specimens was reactive powder concrete (RPC), using local materials and polypropylene microfibers with a compressive strength of 101.79 MPa [1]. RPC is more compact than normal concrete to provide higher compressive strength. This compactness causes brittle behavior, so that addition of microfibers is required to maintain proper ductility. The use of polypropylene microfibers can significantly increase flexural strength, tensile strength and shear strength [2]. All beams of the test specimens were partially pre-stressed

Received April 24th, 2018, Revised December 17th, 2018, Accepted for publication January 11th, 2019.
 ISSN: 2337-5779, DOI: 10.5614/j.eng.technol.sci.2019.51.1.3

reinforced and the columns were fully mild steel reinforced. The loads in the numerical modeling were the same as the loads applied experimentally, i.e. a combination of cyclic lateral and constant axial compressive loads at the top end of the column [1,3]. The experiments were conducted in the Laboratory of Structure and Building Construction, Center of Research and Development on People Housing, Ministry of Public Works and Housing. The numerical models represented three interior beam-column sub-assemblages (SI's) and two exterior beam-column sub-assemblages (SE's) with partial pre-stressed ratio of 33.79% and 22.78%. The numerical modeling used a program that supported finite element analysis.

2 Finite Element Method Model

The ANSYS program was used to perform the finite element analysis of the partially pre-stressed beam-column sub-assemblage numerical models. The RPC, mild steel bars, and pre-stressed strands were numerically modeled using elements that provided appropriate degrees of freedom numbers.

2.1 Finite Element Equation Solution

The relation between strain and nodal displacement is expressed in Eqs. (1) to (3).

$$\{\varepsilon\} = [B]\{u\} \tag{1}$$

where $[B]$ is the strain-displacement matrix based on the element shape function and $\{u\}$ is the node displacement vector.

The relation of stiffness matrix $[K]$ and $[B]$ is as follows:

$$[K] = \int_V [B]^T[D][B]\{u\}dV \tag{2}$$

The relation between stiffness, deformation, and load $\{p\}$ is as follows:

$$[K]\{u\} = \{p\} \tag{3}$$

2.2 Numerical Models

2.2.1 Concrete Numerical Model

In the ANSYS program, the concrete elements were numerically modeled using SOLID65 element as 8-node three-dimensional brick elements [4]. Each node had three degrees of freedom of translation to the X, Y, and Z axes. The SOLID65 element was modeled as an element cracked due to tensile stress, crushed due to compressive stress, plastic deformation, and creep.

a. *Isotropic Condition*

In an isotropic material, the stress matrix $\{\sigma\}$ and strain matrix $\{\varepsilon\}$ are connected by the operator matrix [*D*] as in the following elasticity matrix:

$$\{\sigma\} = [D]\{\varepsilon\} \tag{4}$$

The inverse matrix of elasticity $[D]^{-1}$ is expressed in Eq. (5):

$$[D]^{-1} = \begin{bmatrix} 1/E_x & -\upsilon_{xy}/E_x & -\upsilon_{xz}/E_x & 0 & 0 & 0 \\ -\upsilon_{yx}/E_y & 1/E_y & -\upsilon_{yz}/E_y & 0 & 0 & 0 \\ -\upsilon_{zx}/E_z & -\upsilon_{zy}/E_z & 1/E_z & 0 & 0 & 0 \\ 0 & 0 & 0 & 1/G_{xy} & 0 & 0 \\ 0 & 0 & 0 & 0 & 1/G_{yz} & 0 \\ 0 & 0 & 0 & 0 & 0 & 1/G_{xz} \end{bmatrix} \tag{5}$$

where E_x, ν_{xy}, ν_{yx}, and G_{xy} are the Young modulus on the x-axis, the major Poisson ratio, the minor Poisson ratio, and the shear modulus in the x-y plane, respectively.

b. *Crack Behavior on Concrete Element*

The material stiffness matrix under isotropic material conditions is in Eq. (6) as follows:

$$D^c = \frac{E}{(1+\upsilon)(1-2\upsilon)} \begin{bmatrix} (1-\upsilon) & \upsilon & \upsilon & 0 & 0 & 0 \\ \upsilon & (1-\upsilon) & \upsilon & 0 & 0 & 0 \\ \upsilon & \upsilon & (1-\upsilon) & 0 & 0 & 0 \\ 0 & 0 & 0 & \frac{(1-2\upsilon)}{2} & 0 & 0 \\ 0 & 0 & 0 & 0 & \frac{(1-2\upsilon)}{2} & 0 \\ 0 & 0 & 0 & 0 & 0 & \frac{(1-2\upsilon)}{2} \end{bmatrix} \tag{6}$$

where *E* is the concrete elastic modulus (MPa) and υ is the Poisson ratio of concrete. The matrix of material stiffness based on the stress-strain correlation for materials considered to be cracked in one direction is shown in Eq. (7):

$$D_c^{ck} = \frac{E}{(1+\upsilon)} \begin{bmatrix} \frac{R^t(1-\upsilon)}{E} & \frac{\upsilon}{(1-\upsilon)} & \frac{\upsilon}{(1-\upsilon)} & 0 & 0 & 0 \\ 0 & \frac{1}{(1-\upsilon)} & \frac{\upsilon}{(1-\upsilon)} & 0 & 0 & 0 \\ 0 & \frac{\upsilon}{(1-\upsilon)} & \frac{1}{(1-\upsilon)} & 0 & 0 & 0 \\ 0 & 0 & 0 & \frac{\beta_t}{2} & 0 & 0 \\ 0 & 0 & 0 & 0 & \frac{1}{2} & 0 \\ 0 & 0 & 0 & 0 & 0 & \frac{\beta_t}{2} \end{bmatrix} \tag{7}$$

If the crack is closed due to unloading, the compressive stresses perpendicular to the crack plane will be forwarded to the crack and there is only shear transfer coefficient β_c. Then the stiffness matrix becomes as in Eq. (8):

$$D_c^{ck} = \frac{E}{(1+\upsilon)(1-2\upsilon)} \begin{bmatrix} (1-\upsilon) & \upsilon & \upsilon & 0 & 0 & 0 \\ \upsilon & (1-\upsilon) & \upsilon & 0 & 0 & 0 \\ \upsilon & \upsilon & (1-\upsilon) & 0 & 0 & 0 \\ 0 & 0 & 0 & \frac{\beta_c(1-2\upsilon)}{2} & 0 & 0 \\ 0 & 0 & 0 & 0 & \frac{\beta_c(1-2\upsilon)}{2} & 0 \\ 0 & 0 & 0 & 0 & 0 & \frac{\beta_c(1-2\upsilon)}{2} \end{bmatrix} \quad (8)$$

2.2.2 Mild Steel and Strand Numerical Models

In the ANSYS program, a longitudinal or transversal mild steel bar was numerically modeled using the LINK8 element [4]. The element was formed by two points at the ends of the bar in an X, Y, Z Cartesian coordinate system. Each point had three degrees of freedom of translation toward the X, Y, and Z axes. The element did not resist moment and the stress was assumed to be equal along the bar element. The element's stiffness matrix is as in Eq. (9):

$$[K] = \frac{AE_s}{L} \begin{bmatrix} 1 & 0 & 0 & -1 & 0 & 0 \\ 0 & 0 & 0 & 0 & 0 & 0 \\ 0 & 0 & 0 & 0 & 0 & 0 \\ -1 & 0 & 0 & 1 & 0 & 0 \\ 0 & 0 & 0 & 0 & 0 & 0 \\ 0 & 0 & 0 & 0 & 0 & 0 \end{bmatrix} \quad (9)$$

where A is the cross-sectional area of the element (mm^2), E_s is the steel elastic modulus (MPa), and L is the elemental length (mm).

2.2.3 Bond-Slip Interface Numerical Model in the ANSYS Program

In the ANSYS program input, the stress-strain curves are influenced by bonds between the concrete and the mild steel bars or pre-stressed strands. The interface between the mild steel bars or pre-stressed strands with concrete was numerically modeled using a CONTA178 node to node element with three degrees of freedom of translations toward the X, Y, and Z axes, causing slip (gap) between the concrete and the mild steel bars or pre-stressed strands [4]. The CONTA178 elements were applied along the longitudinal mild steel bars or pre-stressed strands, which resisted compressive and tensile forces under cyclic lateral loads.

The properties of the CONTA178 element are expressed by the curve of bond stress (τ_b) and the strain (ε_b) correlation. The correlation between the concrete strain and the mild steel bar or pre-stressed strand transferred to the concrete around the mild steel bar or pre-stressed strand is expressed in Eq. (10) [5]:

$$\varepsilon_c = \varepsilon_s - \varepsilon_b \quad (10)$$

where ε_c, ε_s, and ε_b are the concrete strains, mild steel bar or pre-stressed strand strain, and mild steel bar or pre-stressed strand strain that are transferred to the concrete around the mild steel bar or pre-stressed strand (bond strain), respectively. If the attachment between the concrete and the mild steel bar or pre-stressed strand is reduced or lost due to cracking of the concrete, then slip occurs. The correlation between concrete cracks and mild steel bar strain or pre-stressed strand strain transferred to the concrete around the mild steel bar or pre-stressed strand is described in Eq. (11):

$$\varepsilon_b = \frac{2\,\delta_b}{C_s} \tag{11}$$

where δ_b, C_s and T are slip length (mm), crack width (mm), and tensile force (Newton), respectively, as shown in Figure 1.

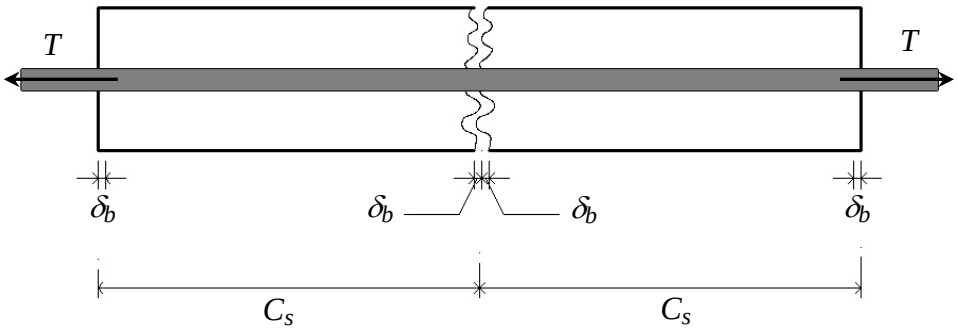

Figure 1 Specimen of concentric tensile test [6].

The crack widths were obtained from the experimental results. The strain conditions due to the loss of attachment can be divided into the following three conditions [7]:

1. The condition $\varepsilon_b \leq \varepsilon_{b0}$. The maximum slip distance when the attachment breaks down is 0.0317 mm [8]. Then the attachment strain of break-down is in Eq. (12)-(15):

$$\varepsilon_{b0} = \frac{63.4 \times 10^{-3}}{C_s} \tag{12}$$

$$\tau_b = [0.0451\, C_s\, \varepsilon_b - 1.07\, (C_s\varepsilon_b)^2 + 12.5(C_s\varepsilon_b)^3 - 58.2(C_s\varepsilon_b)^4]\sqrt{f_c'} \times 10^3 \tag{13}$$

$$E_b = \frac{\tau_b}{\varepsilon_b} \tag{14}$$

$$E_b = \left[0.0451\, C_s - 1.07\, C_s^2\varepsilon_{b0} + 12.5C_s^3\varepsilon_{b0}^2 - 58.2C_s^4\varepsilon_{b0}^3\right]\sqrt{f_c'} \times 10^3 \tag{15}$$

Because:

$$E_b \times \varepsilon_b - \frac{T}{O\ C_s} = 0 \tag{16}$$

$$T = A_s E_s \varepsilon_s \tag{17}$$

then for a pre-stressed strand, if the tensile force that occurs is higher than the initial tensile force in the pre-stressing process, Eq.(17) becomes Eq. (18) as follows:

$$T_p = A_p E_p \varepsilon_p \tag{18}$$

Then:

$$[0.0451\ C_s\ \varepsilon_b - 1.07\ (C_s\varepsilon_b)^2 + 12.5(C_s\varepsilon_b)^3 - 58.2(C_s\varepsilon_b)^4]$$
$$\sqrt{f_c'} \times 10^3 - \frac{T}{O\ C_s} = 0 \tag{19}$$

where ε_{bo}, τ_b, E_b, O, A_s, A_p, E_s, and E_p are bond strain at break-down, concrete stress (MPa), concrete elastic modulus (MPa), circumference of mild steel bar or pre-strand strand cross section (mm), mild steel bar cross section area (mm^2), pre-stressed strand cross-section area (mm^2), elastic modulus (secant) of mild steel bar (MPa), and the elastic modulus (secant) of pre-stressed strand (MPa), respectively.

2. The condition $|\varepsilon_{bo}| < |\varepsilon_b| \leq \delta_1|\varepsilon_{bo}|$, when the attachment starts being damaged. δ_1 is 3.

$$\tau_{b,max} = [0.0451\ C_s\ \varepsilon_b - 1.07\ (C_s\varepsilon_b)^2 + 12.5(C_s\varepsilon_b)^3 - 58.2(C_s\varepsilon_b)^4]\sqrt{f_c'} \times 10^3 \tag{20}$$

$$\varepsilon_c = \frac{O\ C_s\ \tau_{b,max}}{A_s E_s} \tag{21}$$

where ε_c is the concrete strain (constant) and $\tau_{b,max}$ is the maximum attachment stress transferred to the concrete (MPa).

3. The condition $\delta_1|\varepsilon_{bo}| < |\varepsilon_b| \leq \delta_2|\varepsilon_{bo}|$, when the attachment has been damaged. Concrete stress on the descending branch of the stress-strain curve:

$$\tau_{b,slip} = \tau_{b,max}\left[1 - \frac{0.9\ (\varepsilon_b - \delta_1\varepsilon_{b0})}{\varepsilon_{b0}(\delta_2 - \delta_1)}\right]\sqrt{f_c'} \tag{22}$$

$$\varepsilon_c = \frac{O\ C_s\ \tau_{b,slip}}{A_s E_s} \tag{23}$$

where $\tau_{b,slip}$ is the attachment stress when the slip is transferred to the concrete (MPa) and δ_2 is 1.7516.

4. The condition $\delta_2|\varepsilon_{bo}| < |\varepsilon_b|$, when the attachment does not work at all.

$$\tau_b = 0.1\,\tau_{b,max} \tag{24}$$

2.3 Non-linear Equation Numerical Model

The equilibrium equation for a linear system is expressed in Eq. (25) as:

$$[K]\{u\} = \{F^a\} \tag{25}$$

where $[K], \{u\},$ and $\{F^a\}$ are structural stiffness matrix, degrees of freedom vector, and working load vector, respectively.

In nonlinear cases, the Newton-Raphson iteration process is required to solve Eq. (26). It performs iterations for solving each incremental equilibrium:

$$\left[K_i^T\right]\{\Delta u_i\} = \{F^a\} - \{F_i^{nr}\} \tag{26}$$

$$\{u_{i+1}\} = \{u_i\} + \{\Delta u_i\} \tag{27}$$

where $[K_i^T]$, $\{u_i\}$, and $\{F_i^{nr}\}$ are the structural stiffness matrix, degrees of freedom vector, and working load vector, respectively.

For a convergent solution, multiple iterations with the following steps are needed:

1. Assume the value of $\{u_o\}$. Usually, $\{u_o\}$ is the solution of the previous iteration step, then in the first iteration, $\{u_o\} = \{0\}$
2. Create $[K_i^T]$ matrix, $\{F_i^{nr}\}$ from confirmed $\{u_i\}$.
3. Determine $\{\Delta u_i\}$.
4. Add $\{\Delta u_i\}$ to $\{u_i\}$ to obtain $\{u_{i+1}\}$

3 Numerical Modeling of the Test Specimens

Numerical modeling of the three SI and two SE test specimens was conducted using the finite element method. The numerical model inputs referred to the material test results of RPC, mild steel bars and pre-stressed strands, the details of the test specimen dimensions, and the test specimen reinforcement.

3.1 Test Specimen Details

All test specimens were designed to resist seismic loads. The reinforcement of the beams consisted of mild steel bars and pre-stressed strands, while the columns were reinforced by mild steel bars. The partial pre-stressed ratio (PPR) levels on the beams were 22.78% and 33.79% and the strands were placed

unbondedly in the plastic hinge of the beams to reduce strain and slow down the damaging due to cyclic lateral forces [9,10].

The details of the reinforcements are shown in Figures 2, 3, and 4. Each test specimen was placed on a loading frame and resisted loads from vertical and horizontal hydrolic jacks as shown in Figure 5.

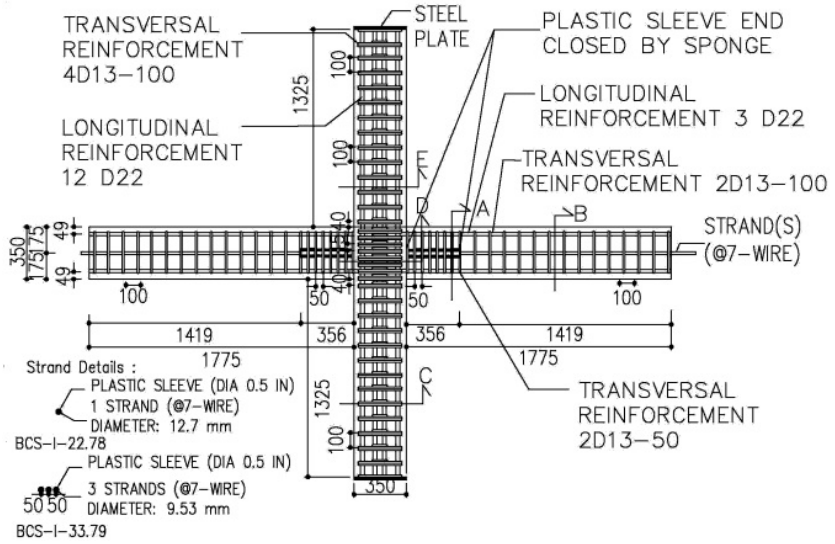

Figure 2 SI-A-33.79, SI-B-33.79, and SI-B-22.78 test specimens [1].

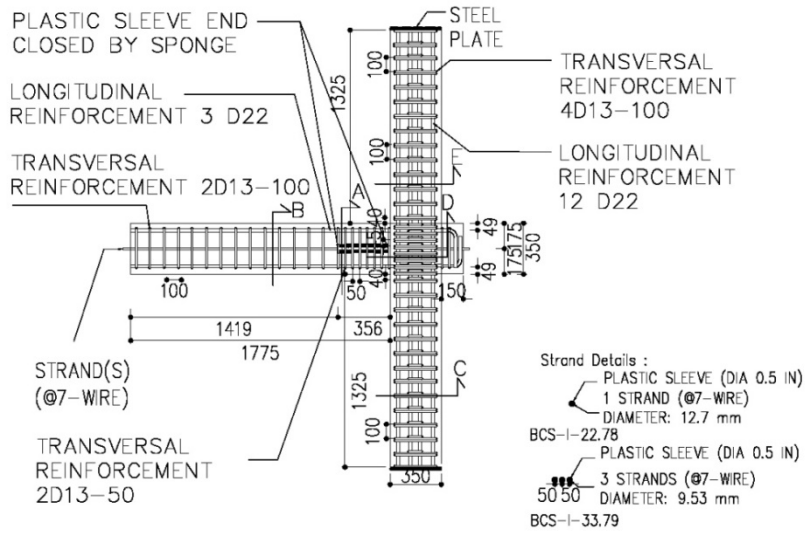

Figure 3 SE-A-33.79 and SE-B-22.78 test specimens [1].

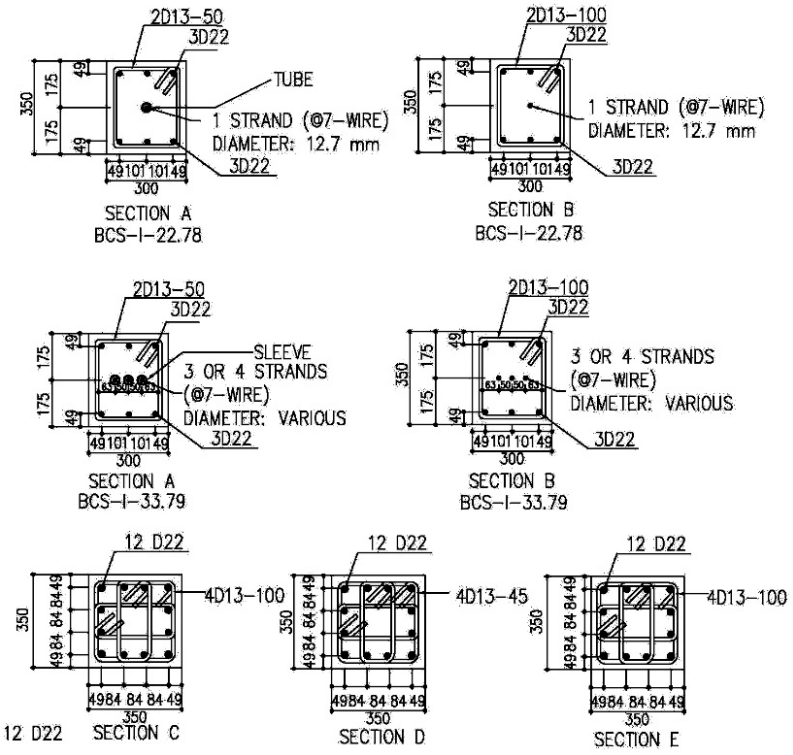

Figure 4 Sections of all test specimens.

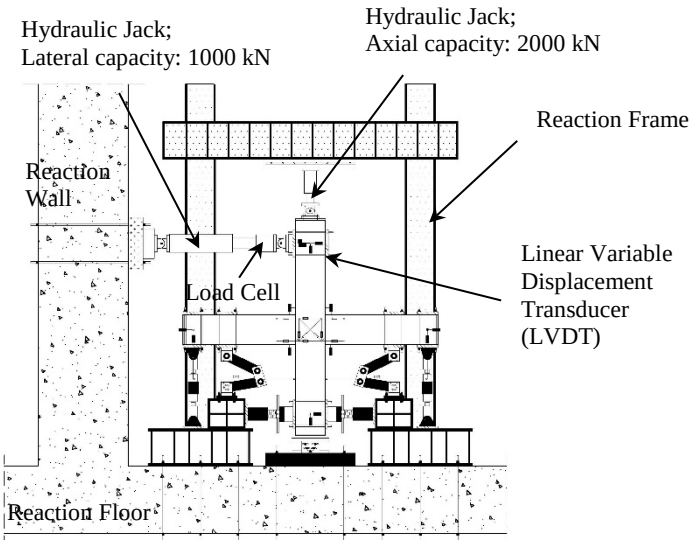

Figure 5 A specimen on the loading frame.

3.2 Numerical Models

Each numerical model had name, dimensions, reinforcement details, and partial pre-stressed ratio (PPR) according to the related test specimen (Table 1). The RPC, mild steel bar, and pre-stressed strand elements on the beam-column sub-assemblages were meshed for finite element analysis.

Front views of all SI and SE numerical models are shown in Figures 6 and 7.

Table 1 Five types of beam-column sub-assemblage numerical models.

Numerical model	Type	Stirrup space on the beam plastic hinges *s* (mm)	PPR (%)
SI-A-33.79	Interior	100	33.79
SI-B-33.79	Interior	50	33.79
SI-B-22.78	Interior	50	22.78
SE-A-33.79	Exterior	100	33.79
SE-B-22.78	Exterior	50	22.78

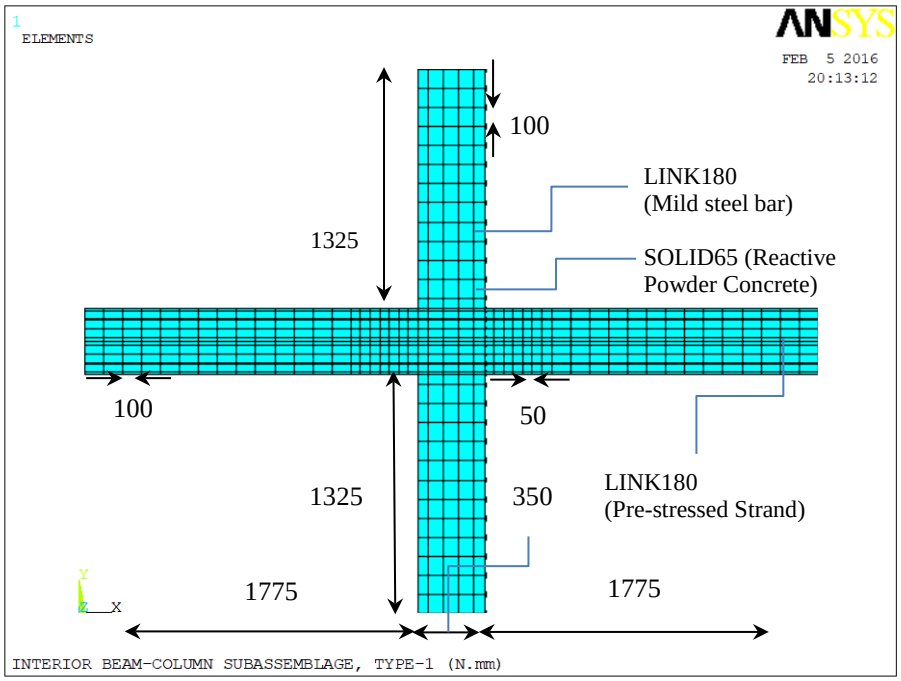

Figure 6 Front view of the beam-column sub-assemblage numerical model's interior (unit: mm).

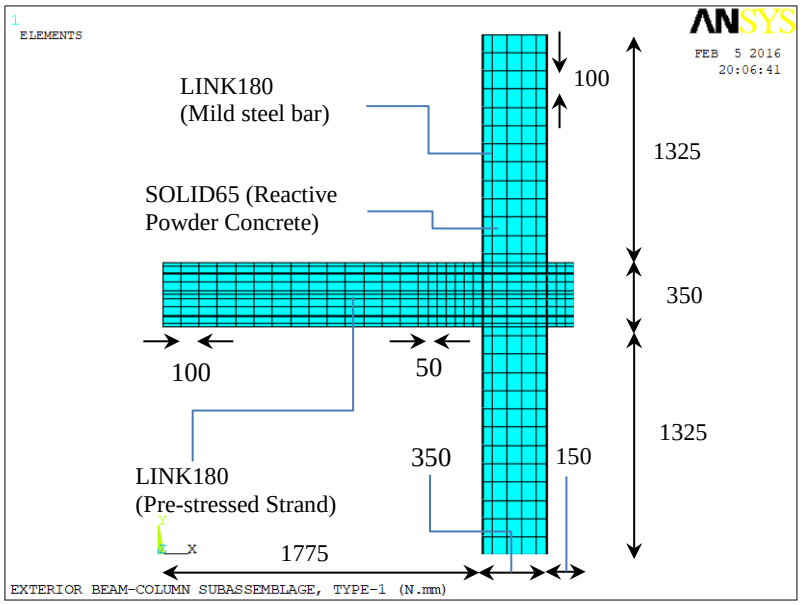

Figure 7 Front view of the beam-column sub-assemblage numerical model's Exterior (unit: mm).

3.3 Loading History

In the numerical modeling, the lateral cyclic loading was based on displacement control [3] and applied only in cycle 1. This was because at each drift ratio, the output of the lateral force-deflection hysteretic curve in cycle 2 and 3 was almost the same as the output of the lateral force-deflection hysteretic curve in cycle 1 [11]. To simplify the analysis, the numerical models were performed only in cycle 1 at each drift ratio, i.e. 0.20, 0.25, 0.35, 0.50, 0.75, 1.00, 1.40, 1.75, 2.20, 2.75, 3.50, and 5.00 percent.

4 Hysteretic Curves

The verification of the numerical models against the experimental results included curve shape and ductility. The hysteretic and backbone curves of all numerical models were relatively the same as those of the experimental results. Figures 8 to 12 show the hysteretic and backbone curves for the lateral force and the displacement relation of the test specimens and the related numerical models. The lateral force differences between the numerical models and the test specimen curves at some high drift ratios were due to the reduced strength and

stiffness of the numerical models. This was caused by the cracked and crushed concrete elements of the numerical models. In this condition, the contribution of the concrete elements in the numerical models to strength and stiffness is decreased significantly [12]. However, the ductility values of the numerical modeling results are close to the experimental results [11].

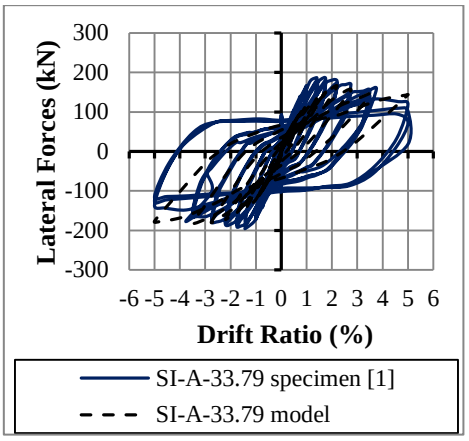

(a) Hysteretic curves of 0% to 5% drift ratio

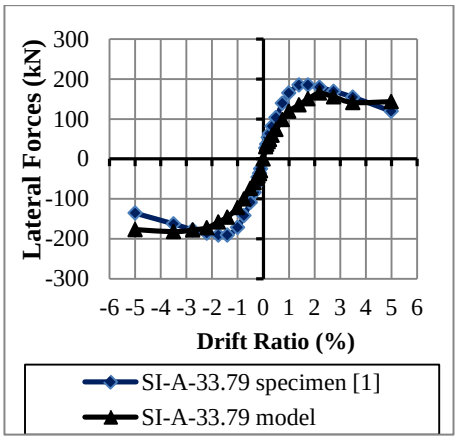

(b) Backbone curves of 0% to 5% drift ratio

Figure 8 Hysteretic and backbone curves of SI-A-33.79 test specimen and numerical model.

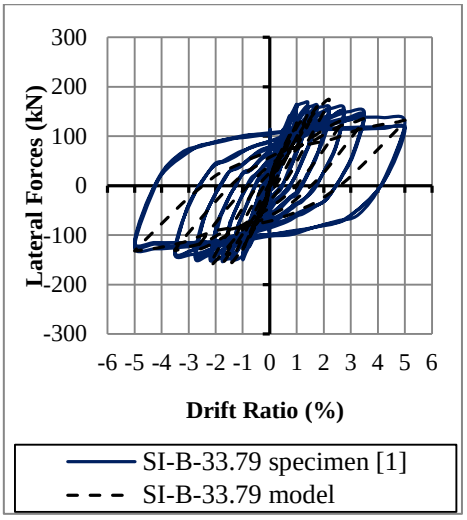

(a) Hysteretic curves of 0% to 5% drift ratio.

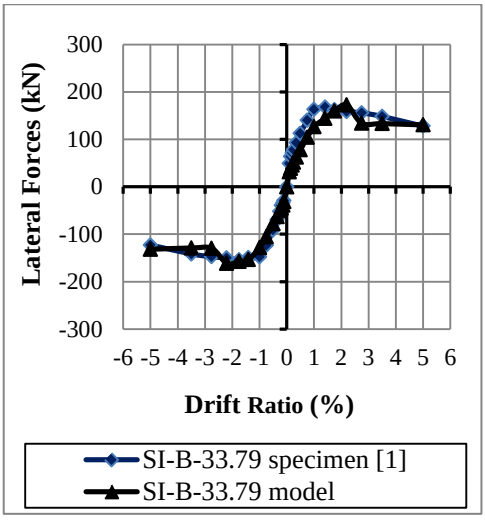

(b) Backbone curves of 0% to 5% drift ratio

Figure 9 Hysteretic and backbone curves of SI-B-33.79 test specimen and numerical model.

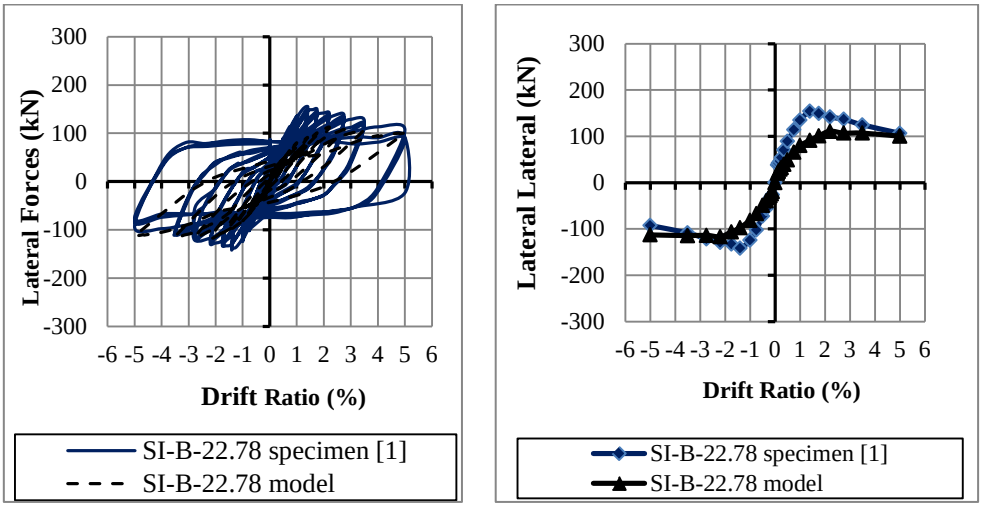

(a) Hysteretic curves of 0% to 5% drift ratio. (b) Backbone curves of 0% to 5% drift ratio.

Figure 10 Hysteretic and backbone curves of SI-B-22.78 test specimen and numerical model.

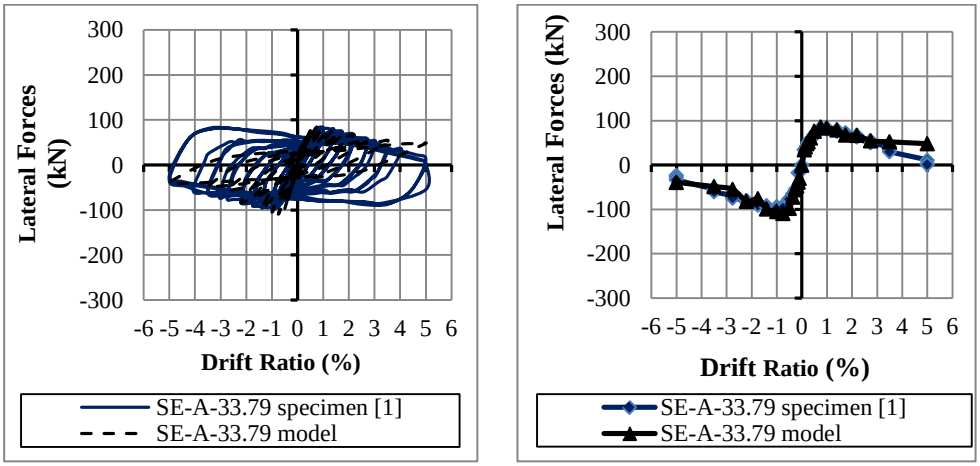

(a) Hysteretic curves of 0% to 5% drift ratio (b) Backbone curves of 0% to 5% drift ratio

Figure 11 Hysteretic and backbone curves of SE-A-33.79 test specimen and numerical model.

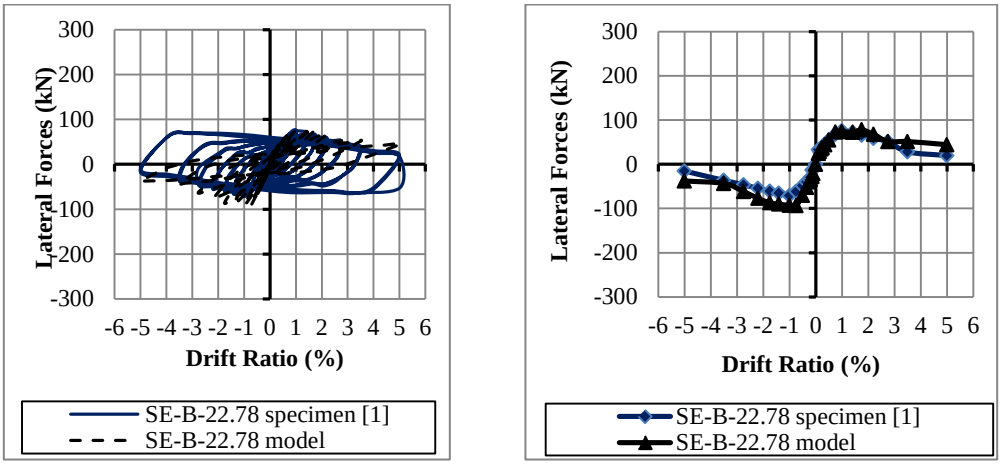

(a) Hysteretic curves of 0% to 5% drift ratio (b) Backbone curves of 0% to 5% drift ratio

Figure 12 Hysteretic and backbone curves of SE-B-22.78 test specimen and numerical model.

5 Stress Distribution

In general, all numerical models began to resist the tensile and the compressive stress at 0.20% drift ratio. The tensile stress was less than 5 MPa, lower than the primary compressive stress and below the average tensile stress value of the material test result of 6.59 MPa. The tensile stress increased along with the drift ratio increment. A diagonal strut action occurred on the joint zone of all SI and SE numerical models at 0.35% drift ratio. Plastic joints on the beams were formed by significantly increased stress. The diagonal strut became wider and increased the stress on the next drift ratios. After peak lateral force, degradation of strength and stiffness set in.

In all SI numerical models there were decreased concrete stresses at the center of the joint zone when the concrete exceeded its peak compressive strength. The low tensile stress of the joint zone centers increased at 5.00% drift ratio. This indicates widespread damage when compared to the conditions of 3.50% drift ratio (Figures 13, 14, and 15). In the SE numerical models, the stress was over 43.89 MPa (dark blue) in the middle of the joint zones and began to spread. The shape of the diagonal strut began to change and spread until 5.00% drift ratio (Figures 16 and 17). The stress on the SE beams was higher than that on the SI beams of the numerical models with the same PPR at 3.50% drift ratio, especially in the plastic hinge areas. This was indicated by the color of the stress contours. The larger stresses led to larger ultimate shear forces on the beams of

the SE test specimens, especially in the plastic hinges. The stress was higher in the SE numerical model, with a PPR of 33.79%, than in the SE numerical model, with a PPR of 22.78%, because of higher lateral forces.

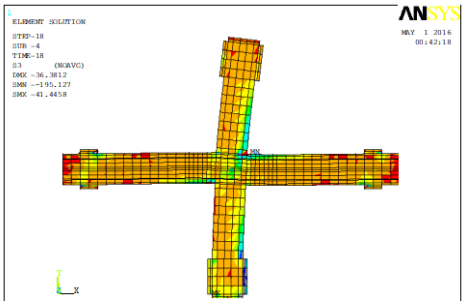

(a) At 1.40% drift ratio: Loading Step (LS)-18; increased stress in the center of the joint zone diagonal strut (light blue) (25.56 to 37.78 MPa)

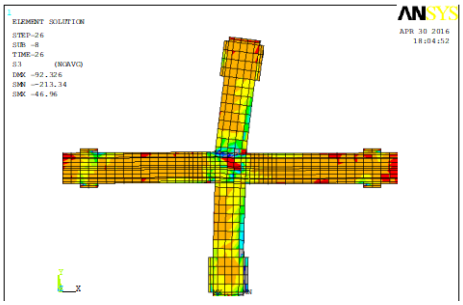

(b) At 3.50% drift ratio: LS-26; decreased compressive stress due to increased concrete damage in the middle of the joint zone (red) (1.11 MPa); continued strength and stiffness degradation

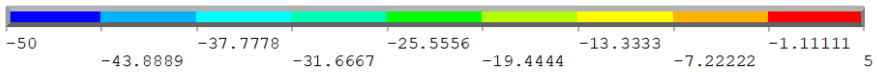

Figure 13 Main stress distribution (σ3) in SI-A-33.79 longitudinal section; push load condition (unit: MPa).

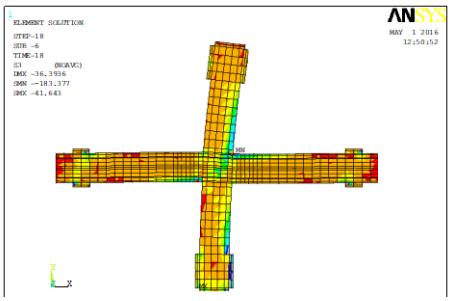

(a) At 1.40% drift ratio: LS-18; increased stress in the center of the joint zone diagonal strut (light blue) (25.56 to 37.78 MPa)

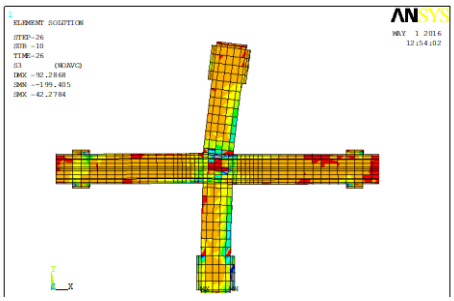

(b) At 3.50% drift ratio: LS-26; decreased compressive stress due to increased concrete damage in the middle of the joint zone (red) (1.11 MPa); continued degradation of strength and stiffness

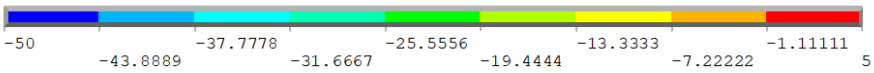

Figure 14 Main stress distribution (σ3) in SI-B-33.79 longitudinal section; push

load condition (unit: MPa).

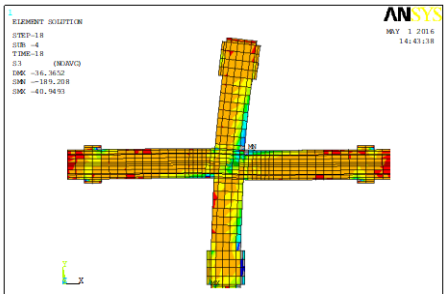

(a) At 1.40 drift ratio: LS-18; increased stress in the center of the joint zone diagonal strut (light blue) (25.56 to 37.78 MPa)

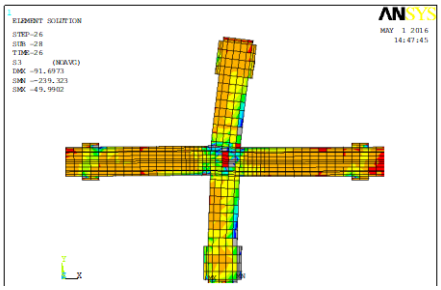

(b) At 3.50% drift ratio: LS-26; decreased compressive stress due to increased concrete break-down in the middle of the joint zone (red); continued degradation of strength and stiffness

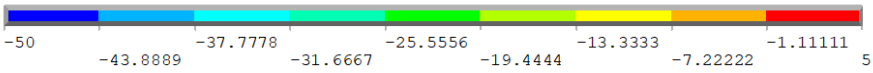

Figure 15 Comparison of primary stress distribution (σ3) in SI-B-22.78 and SE-B-22.78 longitudinal section (unit: MPa).

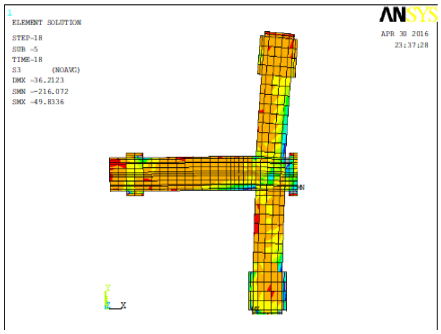

(a) At 1.40% drift ratio: LS-18; increased stress in the center of the joint zone diagonal strut (light blue) (25.56 to 37.78 MPa)

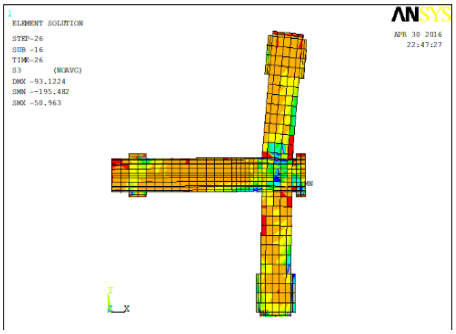

(b) At 3.50% drift ratio: LS-26; the stress above 43.89 MPa (dark blue) in the middle of the joint zone spread; the shape of the diagonal strut started to change and spread at 2.75% drift ratio

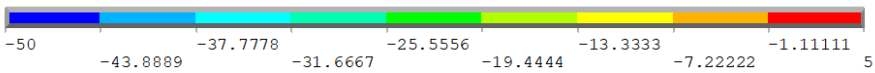

Figure 16 Comparison of primary stress distribution (σ3) in longitudinal section of SE-A-33.79; push load condition (unit: MPa).

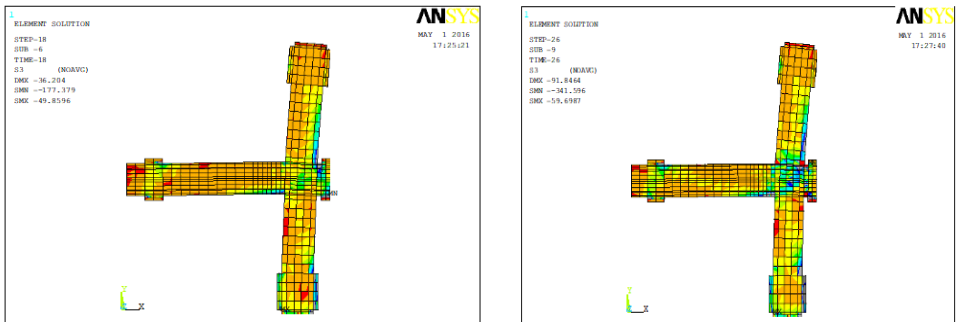

(a) At 1.40% drift ratio: LS-18; increased stress in the center of the joint zone diagonal strut (light blue) (25.56 to 37.78 MPa)

(b) At 3.50% drift ratio: LS-26; the stress above 43.89 MPa (dark blue) in the middle of the joint zone spread; the shape of the diagonal strut started to change and spread at 2.75% drift ratio.

Figure 17 Comparison of primary stress distribution (σ3) in SE-B-22.78 longitudinal section; push load condition (unit: MPa).

The stress distribution contours of all SI numerical models corresponded to the crack patterns in the joint zone of all SI test specimens due to diagonal cracks under cyclic lateral load and damage in the center of the joint zones (Figures 18(a-c)). The compressive stress on the joint zone increased and did not reach peak compressive stress until the end of loading in all SE numerical models. This corresponds to the crack patterns of the joint zones of all SE test specimens, as there were only a few hair cracks (Figures 18(d-e)).

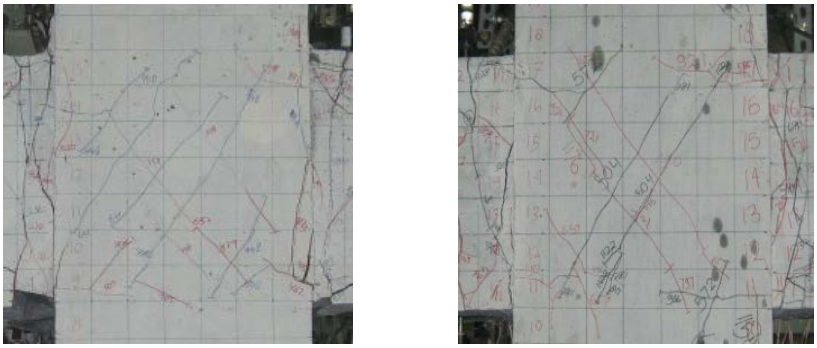

(a) SI-A-33.79 (b) SI-B-33.79

Figure 18 Crack patterns in the joint zone of test specimens.

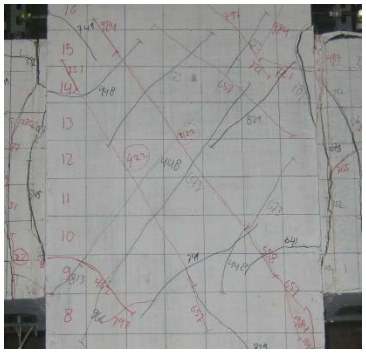

(c) SI-B-22.78

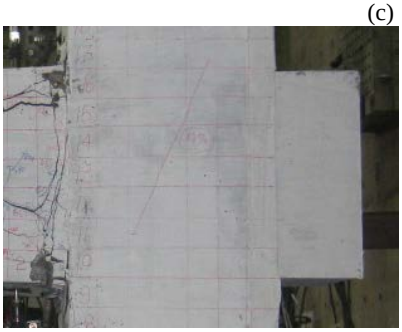

(d) SE-A-33.79

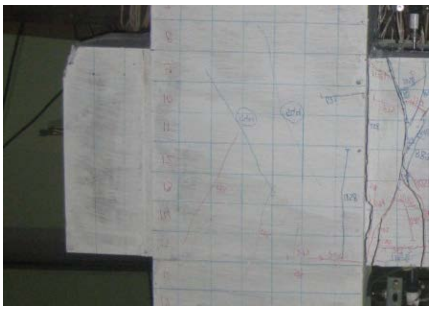

(e) SE-B-22.78

Figure 18 ***Continued.*** Crack patterns in the joint zone of test specimens.

6 Conclusions

From the numerical modeling results it can be concluded that the hysteretic and backbone curves of the numerical models showed good similarity with the test specimen curves. The differences were caused by stiffness and strength degradation due to cracking and crushing of the concrete elements in the numerical models. This condition made the contribution to strength and stiffness of the concrete elements in the numerical models decrease significantly. However, the numerical model results showed values of ductility that were close to those from the experimental results.

The modeling of test specimens with numerical analysis showed a correlation between each numerical model and the related test specimen. The diagonal strut shapes and stress distributions in the numerical models performed similarly as the crack patterns in the test specimens. The stress distribution showed that diagonal strut action formed in the joint zones from the beginning of loading in all SI and SE numerical models. The stress continued to increase according to the loading history. After achieving peak lateral force, the behavior of the SI numerical models began to differ from the SE numerical models. In the SI

numerical models, the diagonal strut shapes changed due to spread stress on the joint zones, which were followed by decreased stress and then relatively constant stress. This corresponded to the crack patterns in all SI test specimens because there were many diagonal cracks in the joint zones due to the diagonal strut action. The stress continued to increase and then became relatively constant. It did not achieve maximum stress in all SE numerical models. This corresponded to the crack patterns in all SE test specimens since there were almost no diagonal cracks in the joint zones because the maximum stress was not achieved.

7 Recommendations

Numerical modeling of crack patterns to be compared with experimental results can be used to predict the failure behavior of test specimens. Moreover, to improve the numerical modeling, finer concrete element dimensions are required to avoid premature stiffness and strength degradation due to cracked and crushed concrete elements, which significantly decrease the strength and stiffness in the numerical models.

Acknowledgements

This study was supported by PT Wijaya Karya Beton, Indonesia under a joint research with the Faculty of Civil and Environment Engineering, Institut Teknologi Bandung.

References

[1] Nurjannah, S.A., Budiono, B., Imran, I. & Sugiri, S., *The Hysteretic Behavior of Partially Pre-Stressed Beam-Column Joint Sub-Assemblages Made of Reactive Powder Concrete*, Journal of Engineering and Technological Sciences. **48**(5), pp. 550-570, 2016.

[2] Patel, P.A., Desai, A.K. & Desai, J.A., *Evaluation of Engineering Properties for Polypropylene Fiber Reinforced Concrete*, International Journal of Advanced Engineering Technology, **III**(I), Jan-March, pp. 42-45, 2012.

[3] ACI Committee, *Acceptance Criteria for Moment Frames Based on Structural Testing and Commentary*, ACI 374.1-05, F. Hills, USA, 2005.

[4] ANSYS v. 17.0, program manual, 2018.

[5] Foster, S.J. & Gilbert, R.I., *A Discrete Bond-Slip Element for Use in Modelling Reinforced Concrete Structures*, the 6th International Conference in Australia on FEM, pp.167-172, Sydney, July 8th-10th, 1991.

[6] Nilson, A.H., *Bond Stress-Slip Relations in Reinforced Concrete*, Research Report No. 345, Department of Structural Engineering, Cornell University, pp. 40, December, 1971.
[7] Budiono, B., *Hysteretic Behavior of Partially-prestressed Concrete Beam-column Connection*s, Ph.D. Dissertation, Department of Structural Engineering, School of Civil Engineering, University of New South Wales, Australia, 1995.
[8] Houde, J. & Mirza, M.S., *A Finite Element Analysis of Shear Strength of Reinforced Concrete Beams*, ACI Journal, SP42-5, **1**, pp. 103-128, 1974.
[9] BSN, SNI 03-2847-2013 *The Design Method of Concrete Structure for Buildings*, Jakarta, 2013. (Text in Indonesian)
[10] ACI Committee, *Building Code Requirements for Structural Concrete* (ACI 318-14) and Commentary, ACI, Farmington Hills, USA, 2014.
[11] Nurjannah, S. A., *Hysteretic Behavior of Partially Pre-stressed Reactive Powder Concrete Beam-column Sub-assemblages*, Dissertation in Post Graduate of Civil Engineering Program, Institut Teknologi Bandung, Indonesia, pp. 371, 2016. (Text in Indonesian)
[12] Kurniawan, R. *The Behavior of Reactive Powder Concrete Plate-Column Connection under Gravity and Cyclic Lateral Loads*, Doctoral Dissertation, Civil Engineering Program, Institut Teknologi Bandung, Indonesia, 2015. (Text in Indonesian)